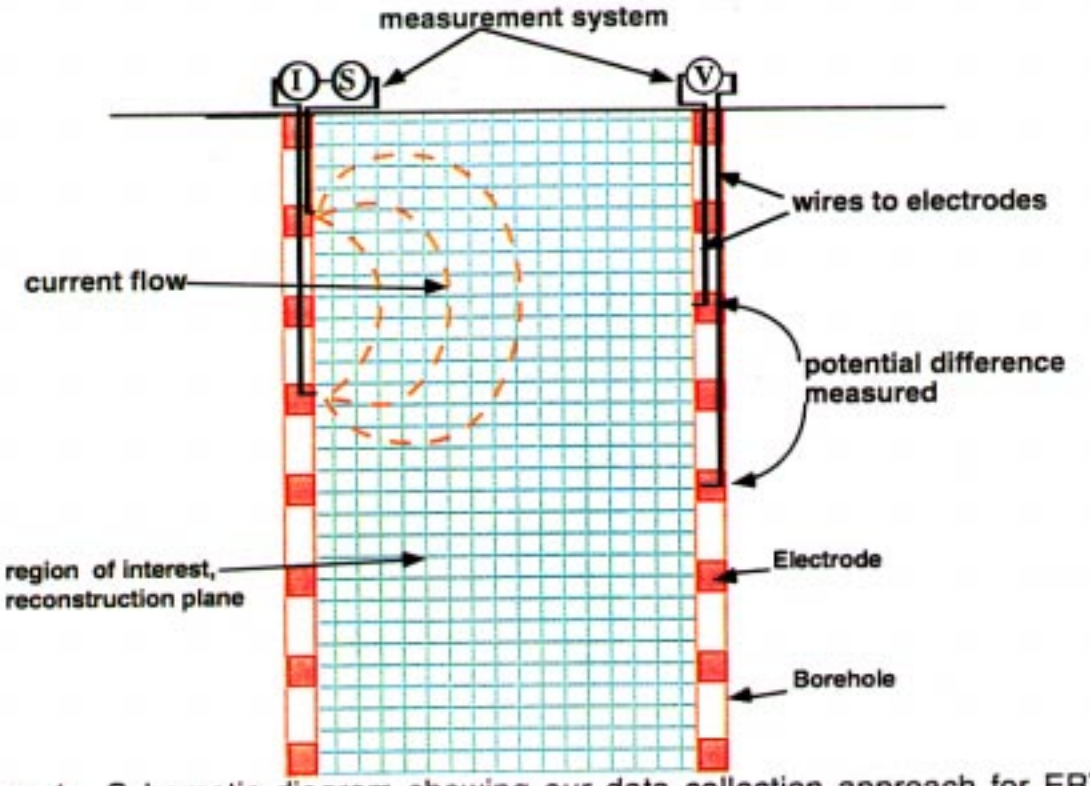

Figure 1. Schematic diagram showing our data collection approach for ERT measurements, where I = source current, S = signal source, and V = voltage. Electrodes in each borehole make electrical contact with the formation. Current is driven through the formation from two electrodes and the potential difference is measured between other electrode pairs. The procedure is repeated for many combinations of source and receiver electrode positions in the same borehole or in different boreholes.

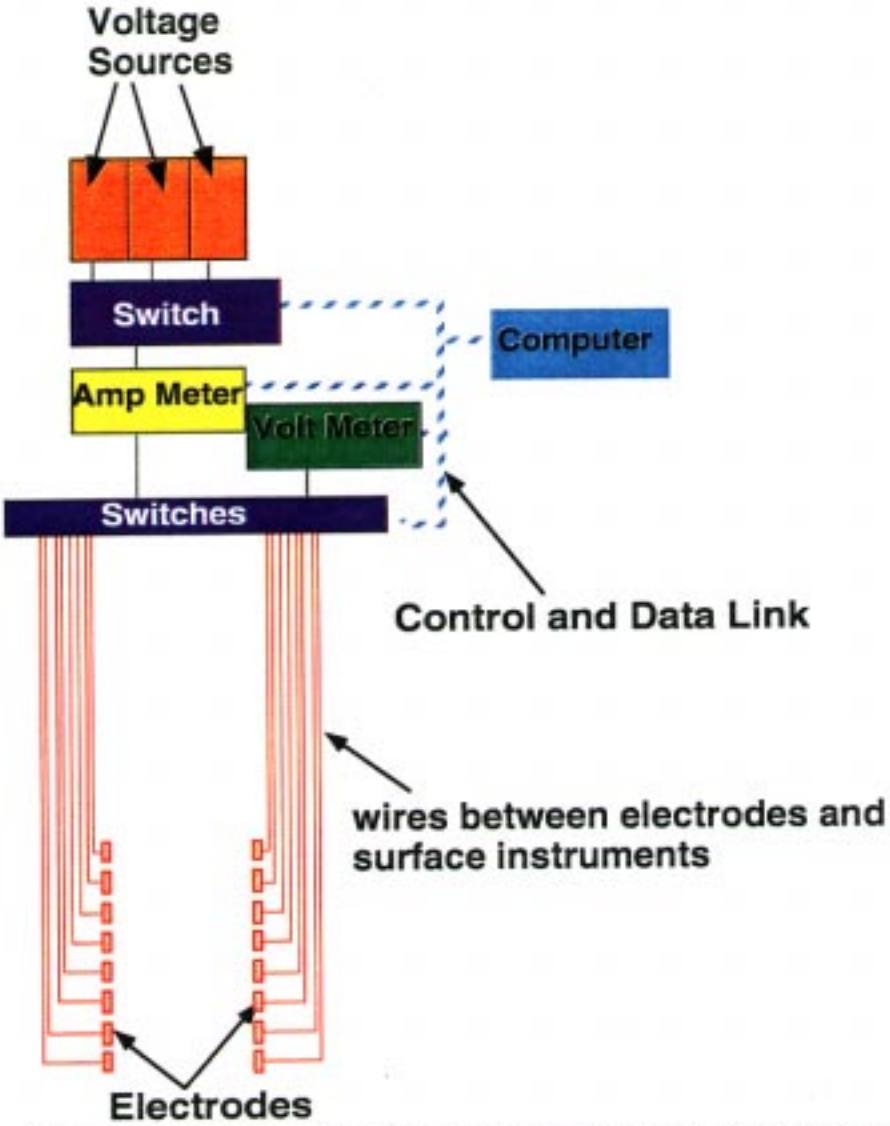

Figure 2. Schematic diagram showing the computer controlled data acquisition and switching system used to collect the ERT data.

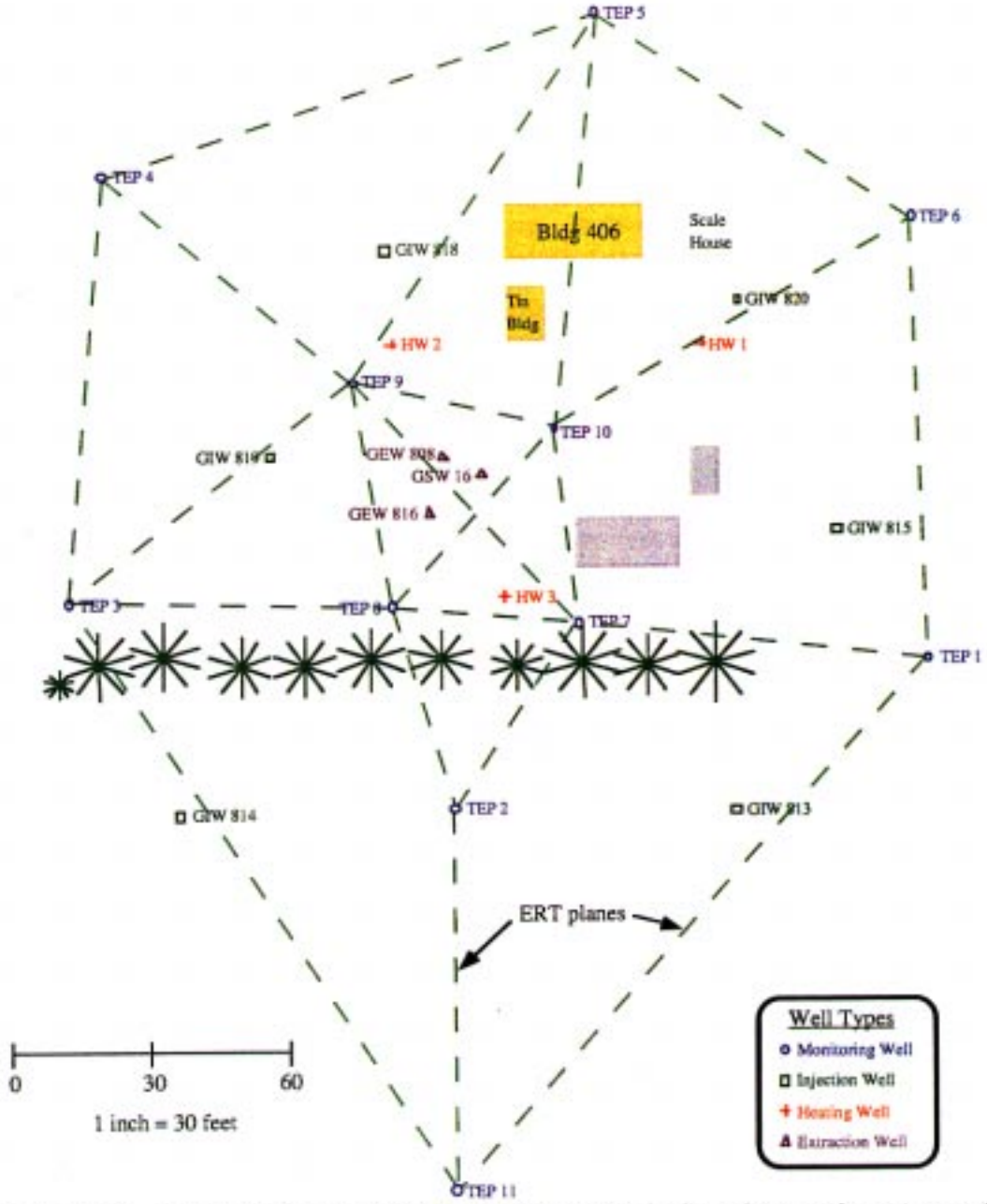

Figure 3. This plan view of the experimental site shows the steam injection gas/liquid extraction wells, ohmic heating wells and boreholes used to monitor both thermal processes; eleven vertical boreholes were drilled nearby to monitor changes in soil resistivity and temperature during the course of remedial action.

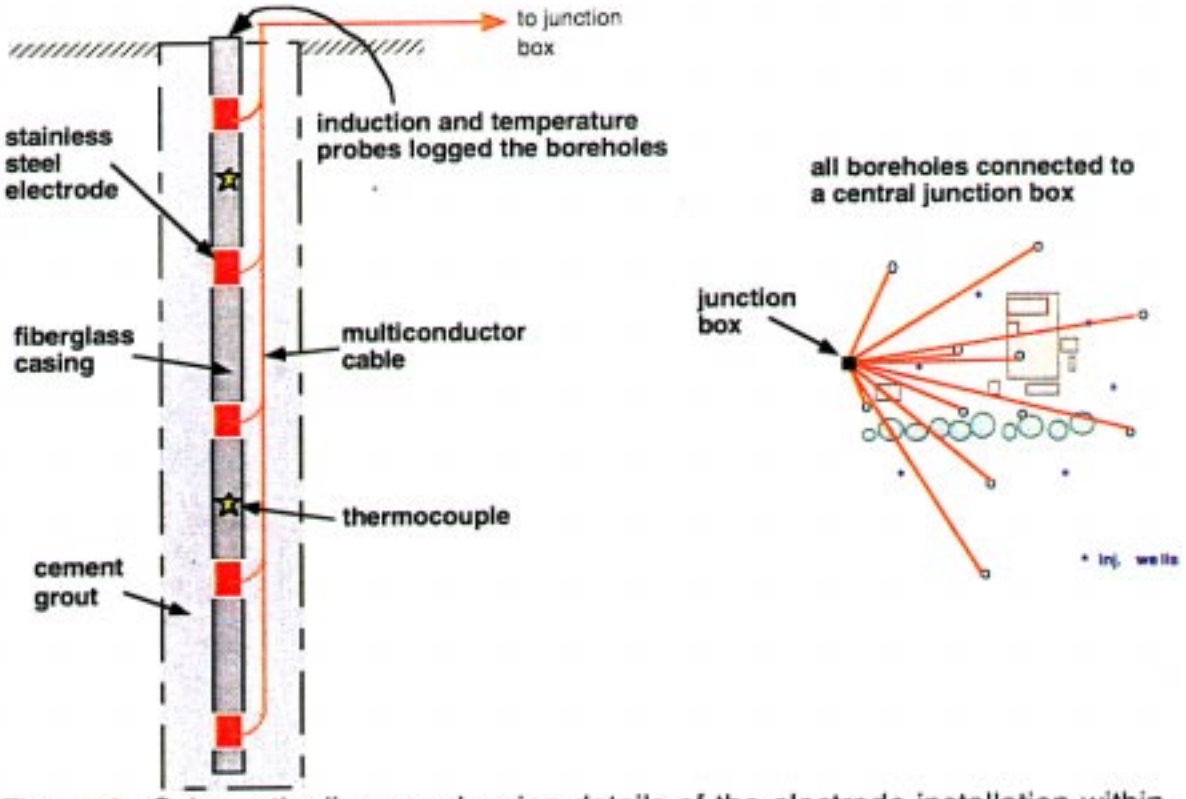

Figure 4. Schematic diagram showing details of the electrode installation within the ERT wells. The diagram is not to scale.

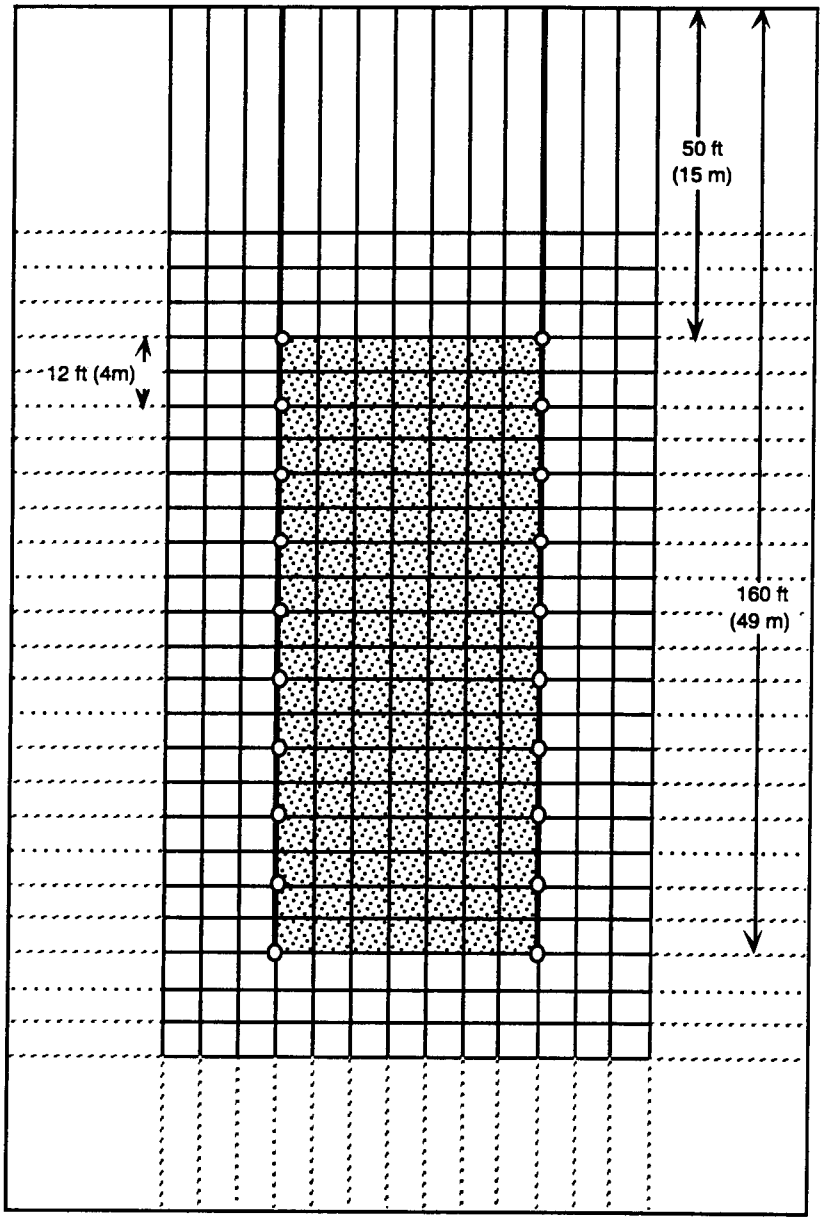

Figure 5a. Reconstruction planes defined by boreholes separated by less than 18 m were modeled by a finite element mesh 7 elements wide (between the boreholes) and 18 elements long (along the boreholes). The image plane height was in all cases 32 m (108 ft.). The width ranged from 12.5 to 17.8 m (41-59 ft.)

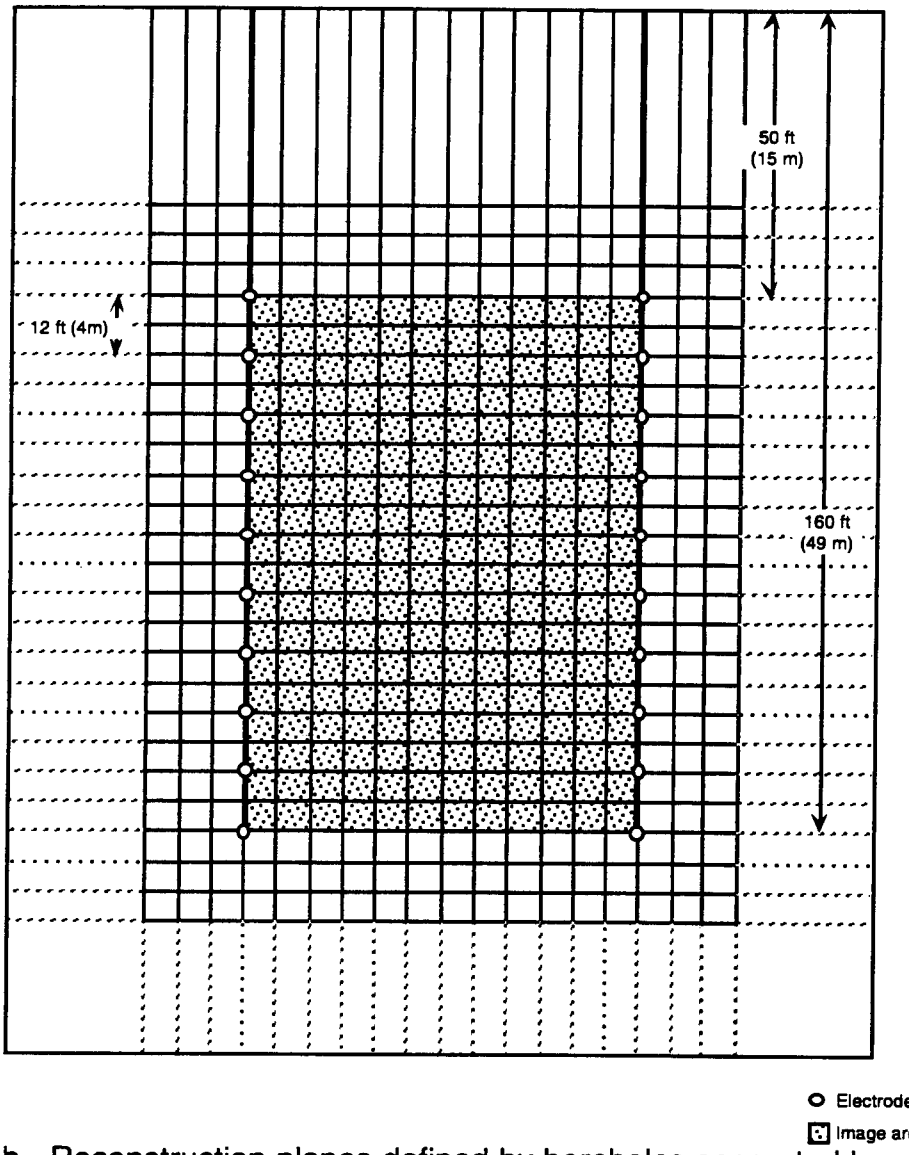

Figure 5b. Reconstruction planes defined by boreholes separated by more than 18 m were modeled by a finite element mesh 12 elements wide (between the boreholes) and 18 elements long (along the boreholes). The image plane height was in all cases 32 m (108 ft.). The widths ranged from 20.9 to 48 m (69 -158 ft.)

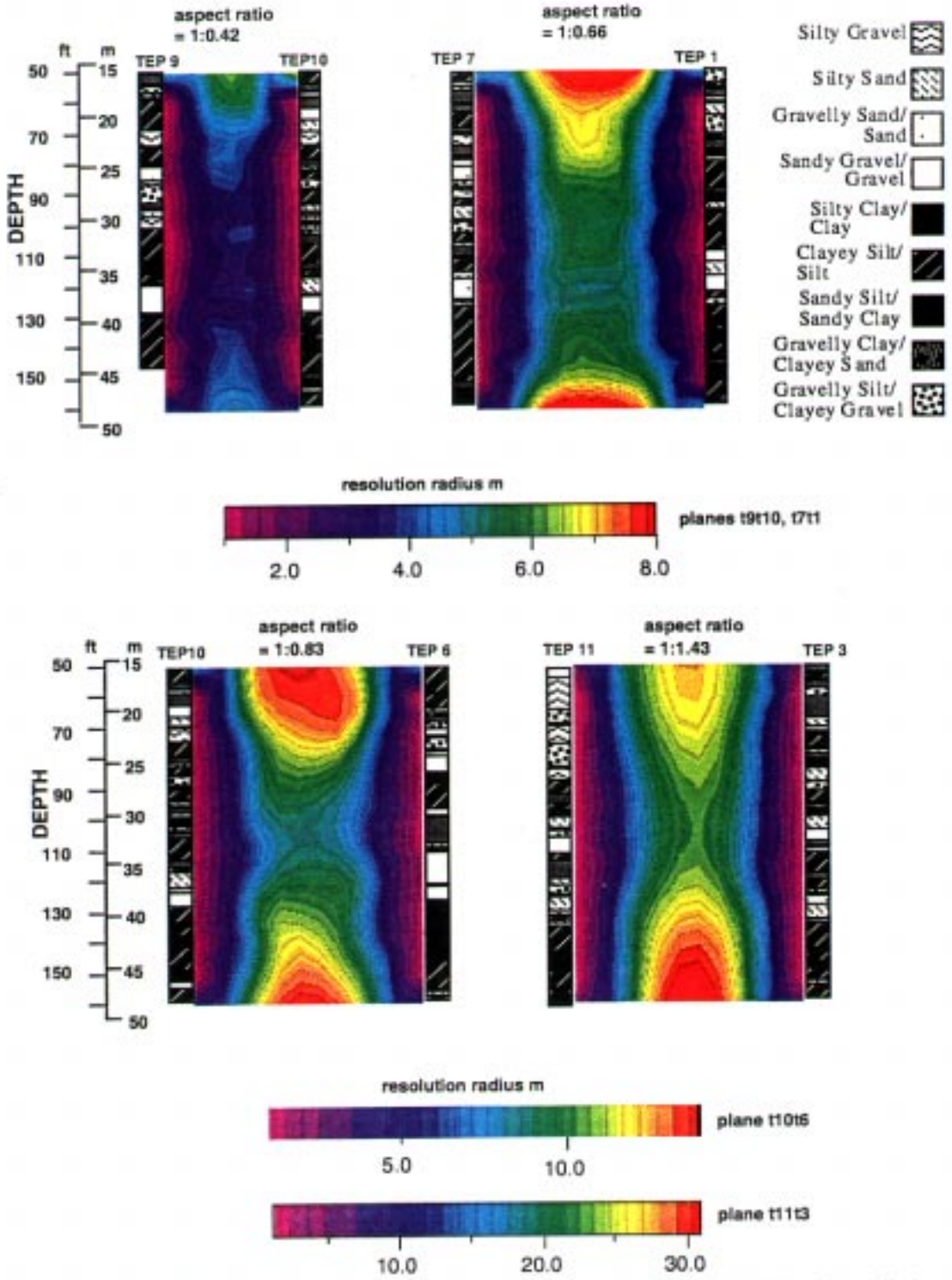

Figure 6. Images depicting the resolution radius matrices in meters for all the reconstruction planes. Resolution radius is defined as the distance over which the inversion averages the resistivity values. The ratio of vertical to horizontal spatial scale varies between individual images.

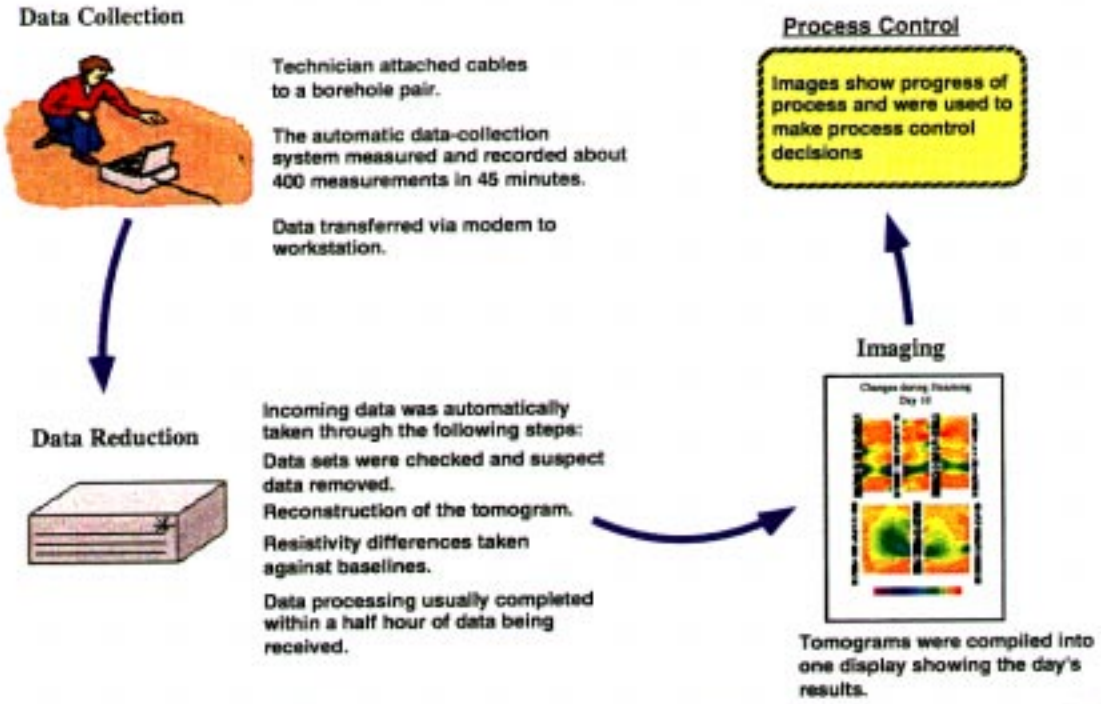

Figure 7 summarizes the key elements of the data collection and data processing systems used to produce ERT tomographs in near-real time.

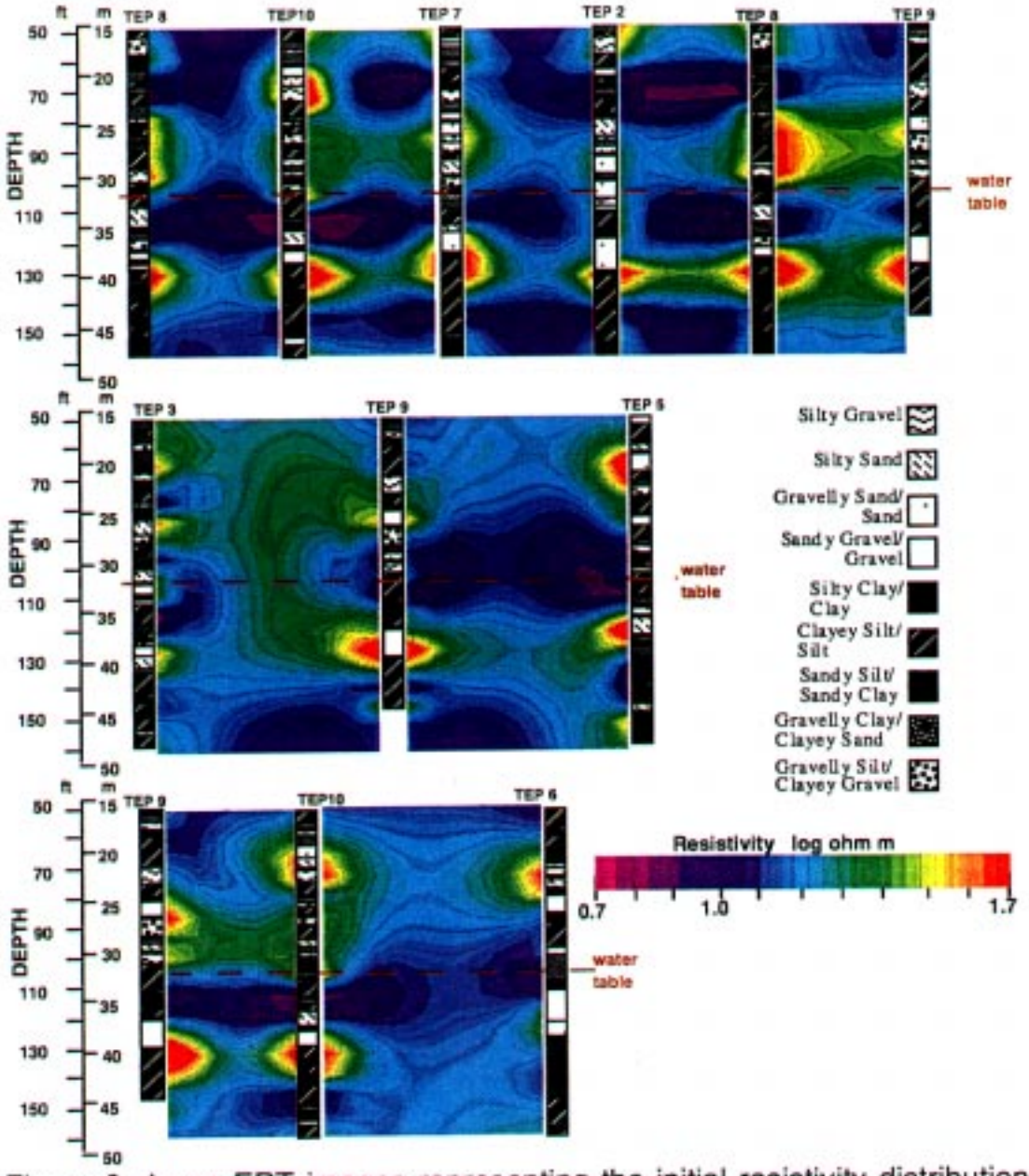

Figure 8 shows ERT images representing the initial resistivity distributions for the experimental site. The image are compared with lithologic logs based on the geologist's description of core from the corresponding boreholes.

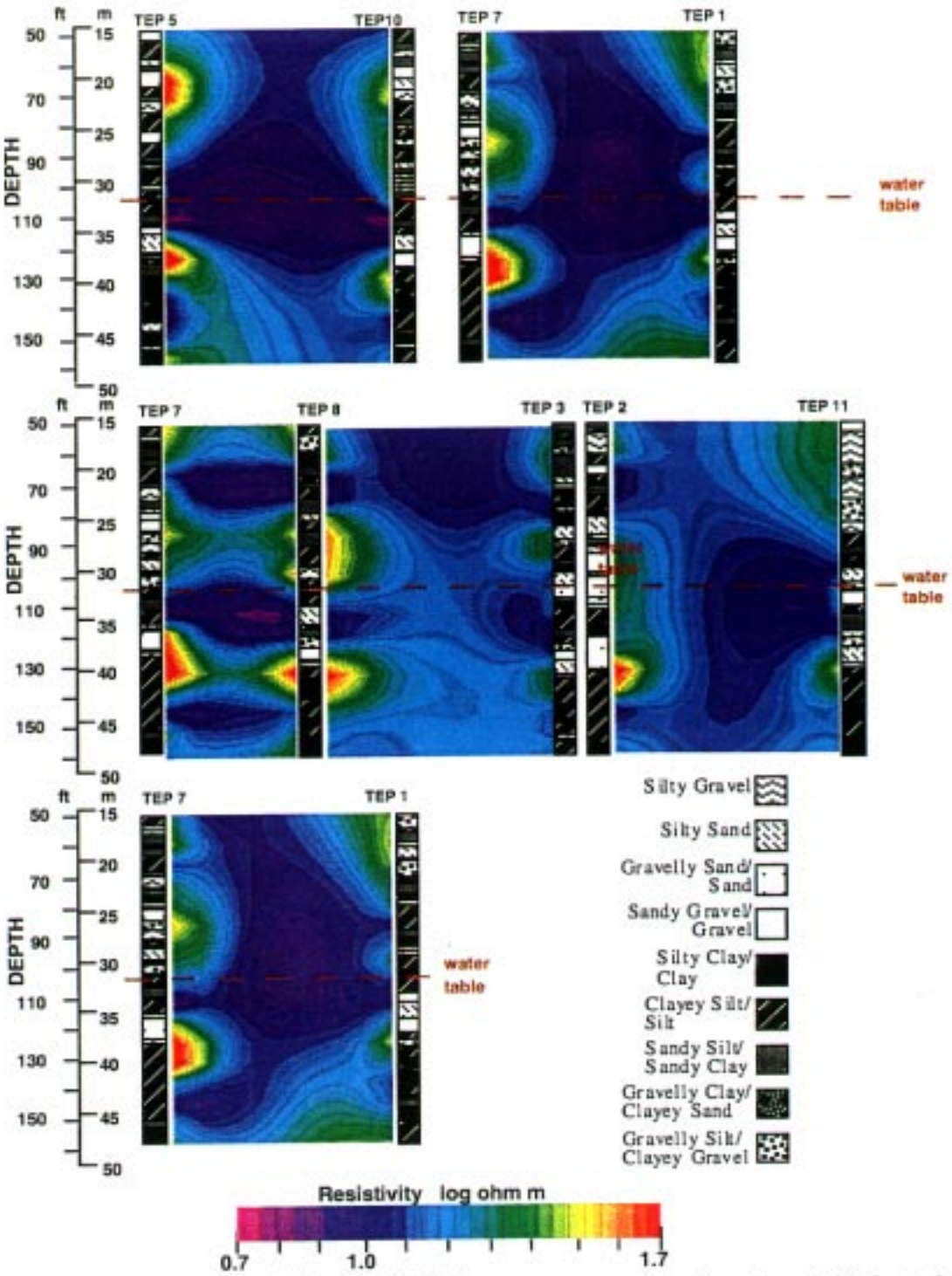

Figure 8b shows additional ERT images representing the initial resistivity distributions for the experimental site. The image are compared with lithologic logs based on the geologist's description of core from the corresponding boreholes.

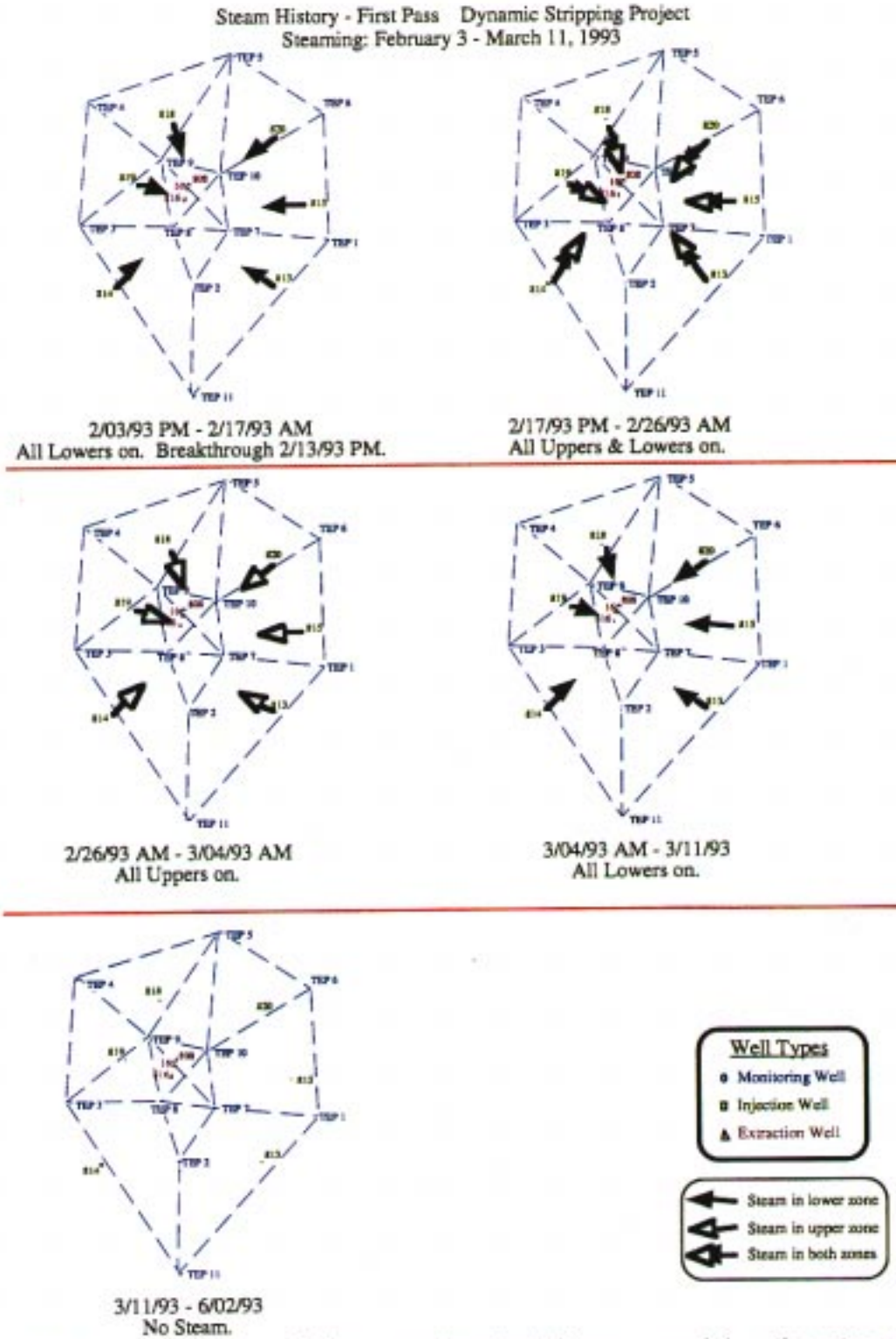

Figure 9. Plan view of the experimental site summarizing the steam injection schedule used during the first steam injection cycle.

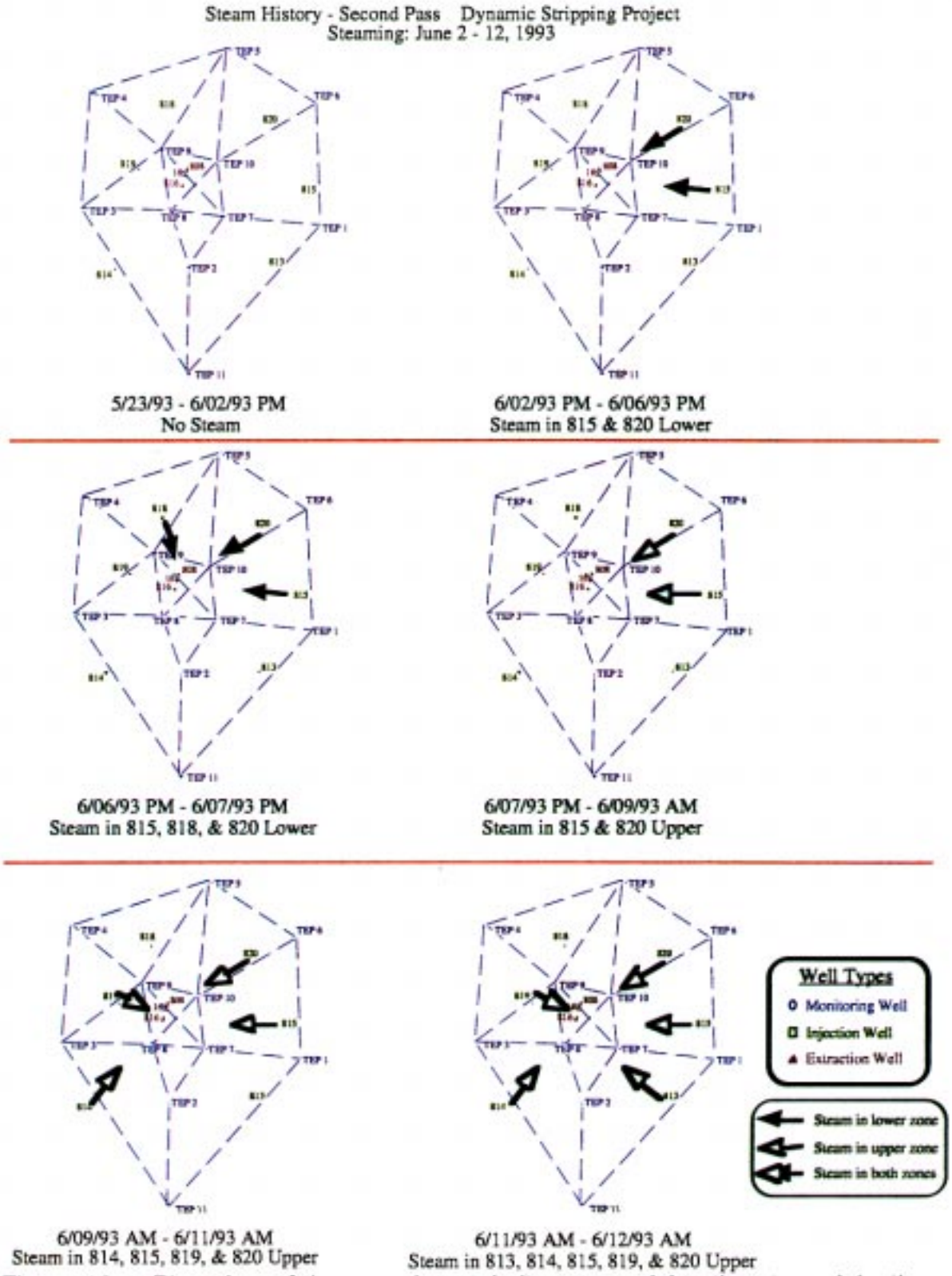

Figure 10a. Plan view of the experimental site summarizing the steam injection schedule used during the first half of the second steam injection cycle.

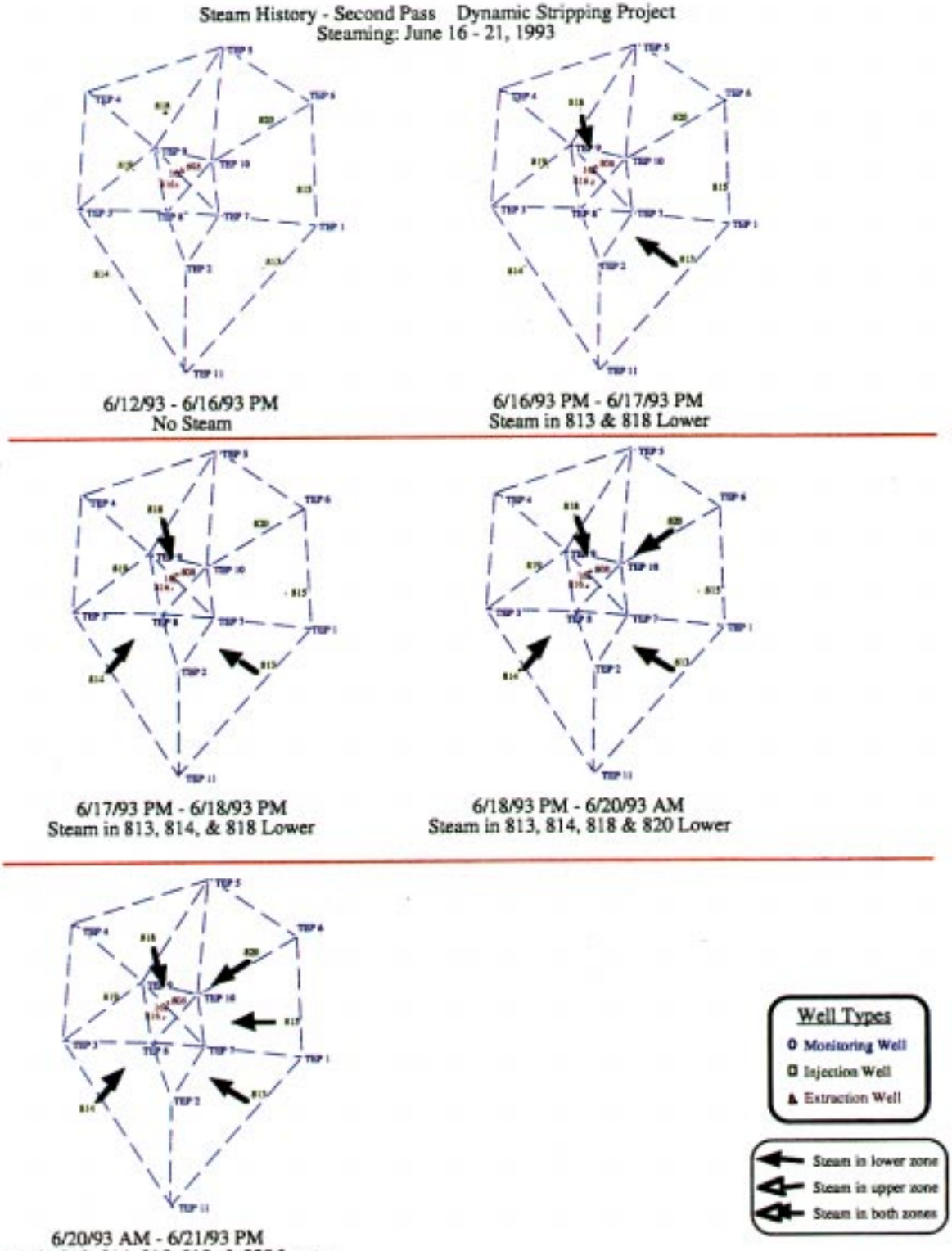

Figure 10b. Plan view of the experimental site summarizing the steam injection schedule used during the second half of the second steam injection cycle.

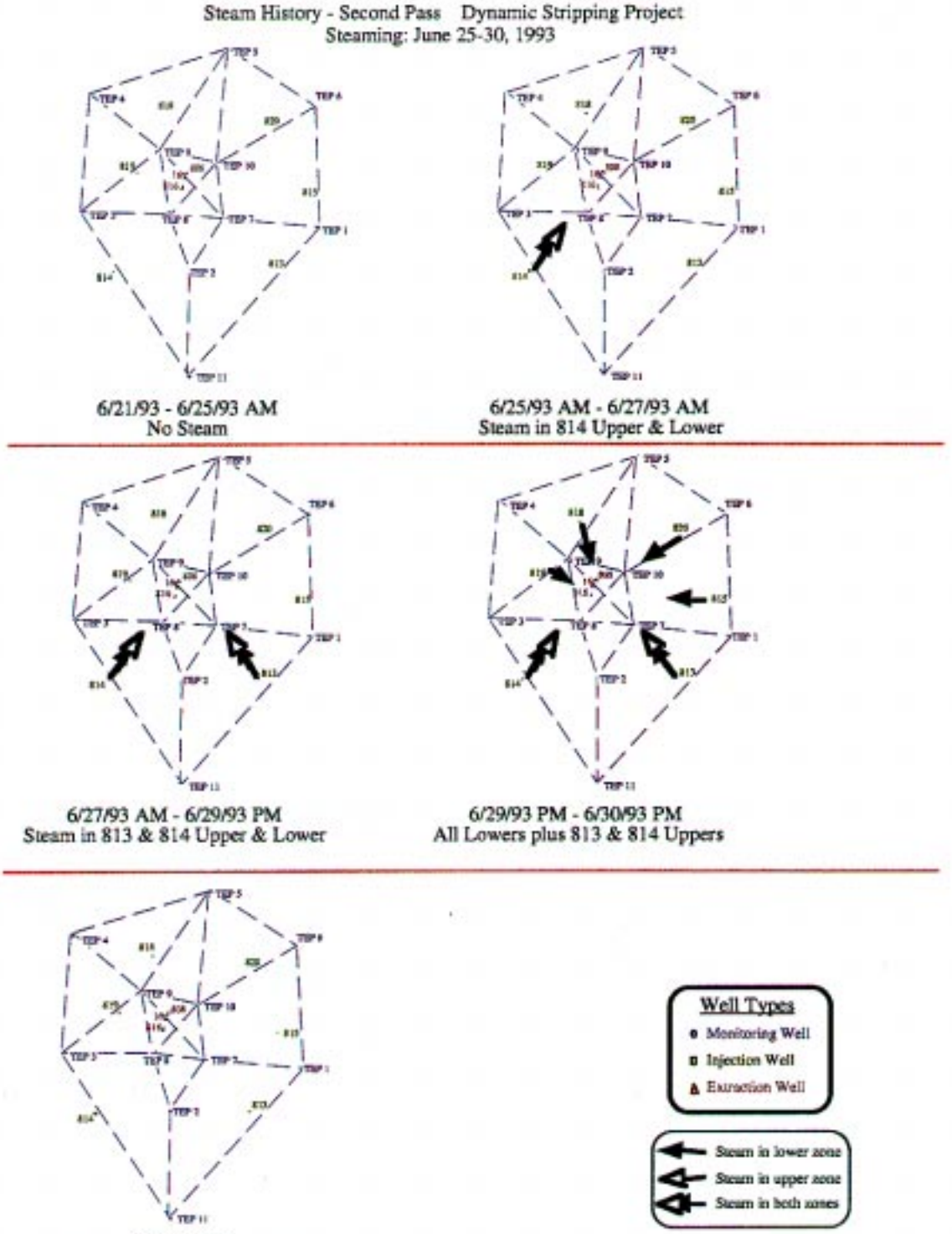

Figure 10b. Plan view of the experimental site summarizing the steam injection schedule used during the second half of the second steam injection cycle.

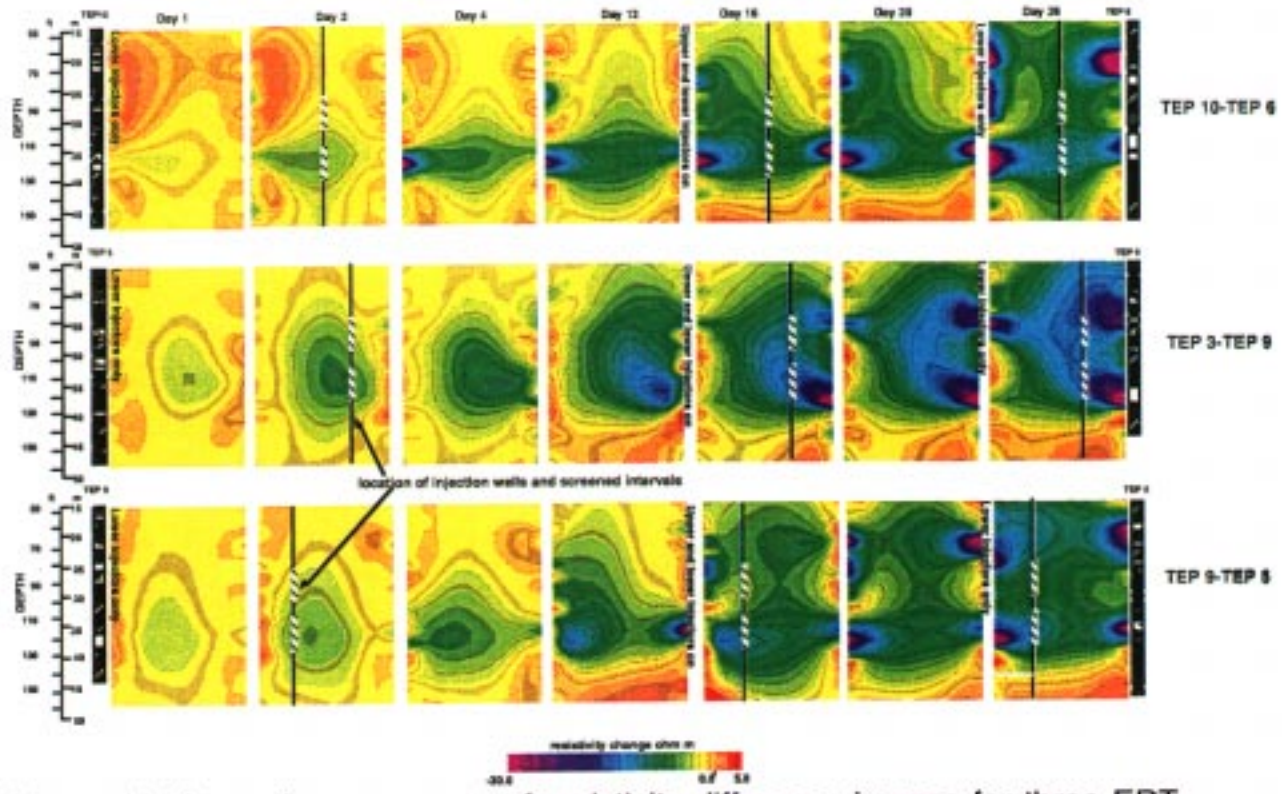

Figure 11 shows time sequence of resistivity difference images for three ERT planes located in close proximity to three steam injection wells. The resistivity changes shown by the images can be used to map the progress of the steam flood. The location of the injection wells and screened horizons is also shown for comparison.

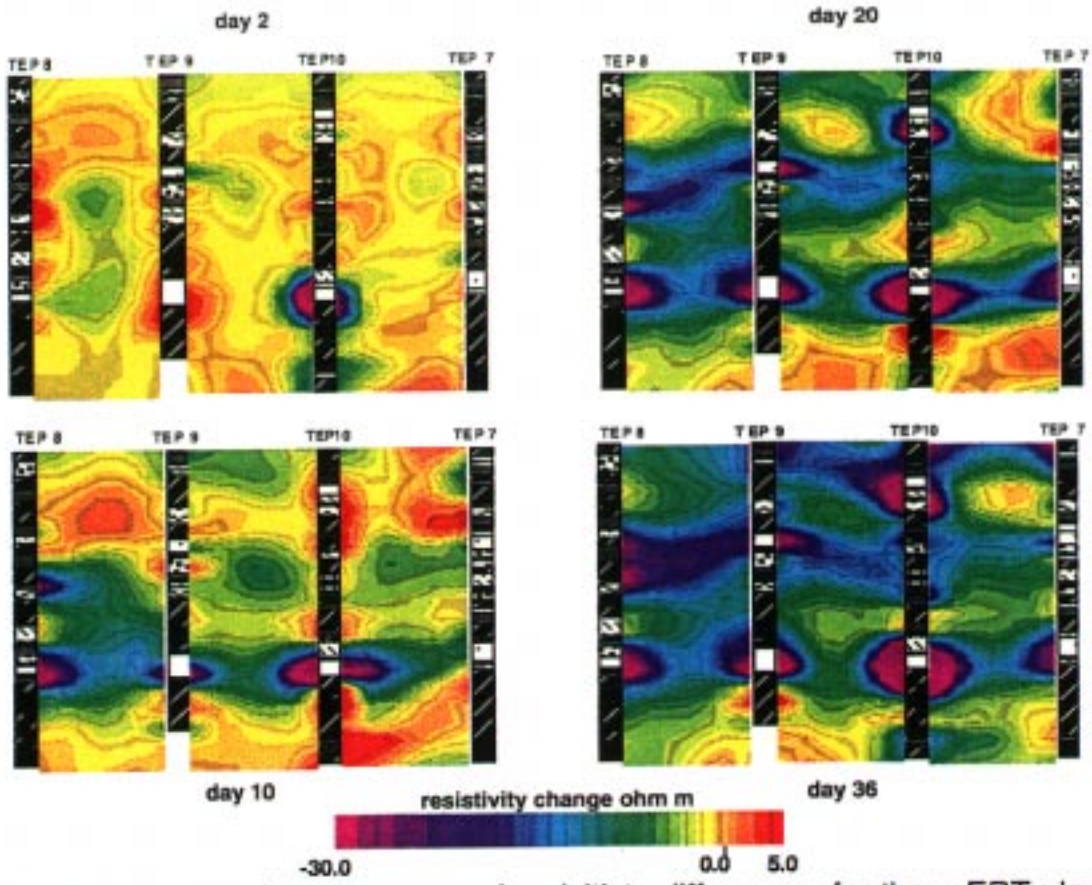

Figure 12 shows a time sequence of resisitivty differences for three ERT planes located near the center of the injection area. The time labels indicate the time since the start of injection.

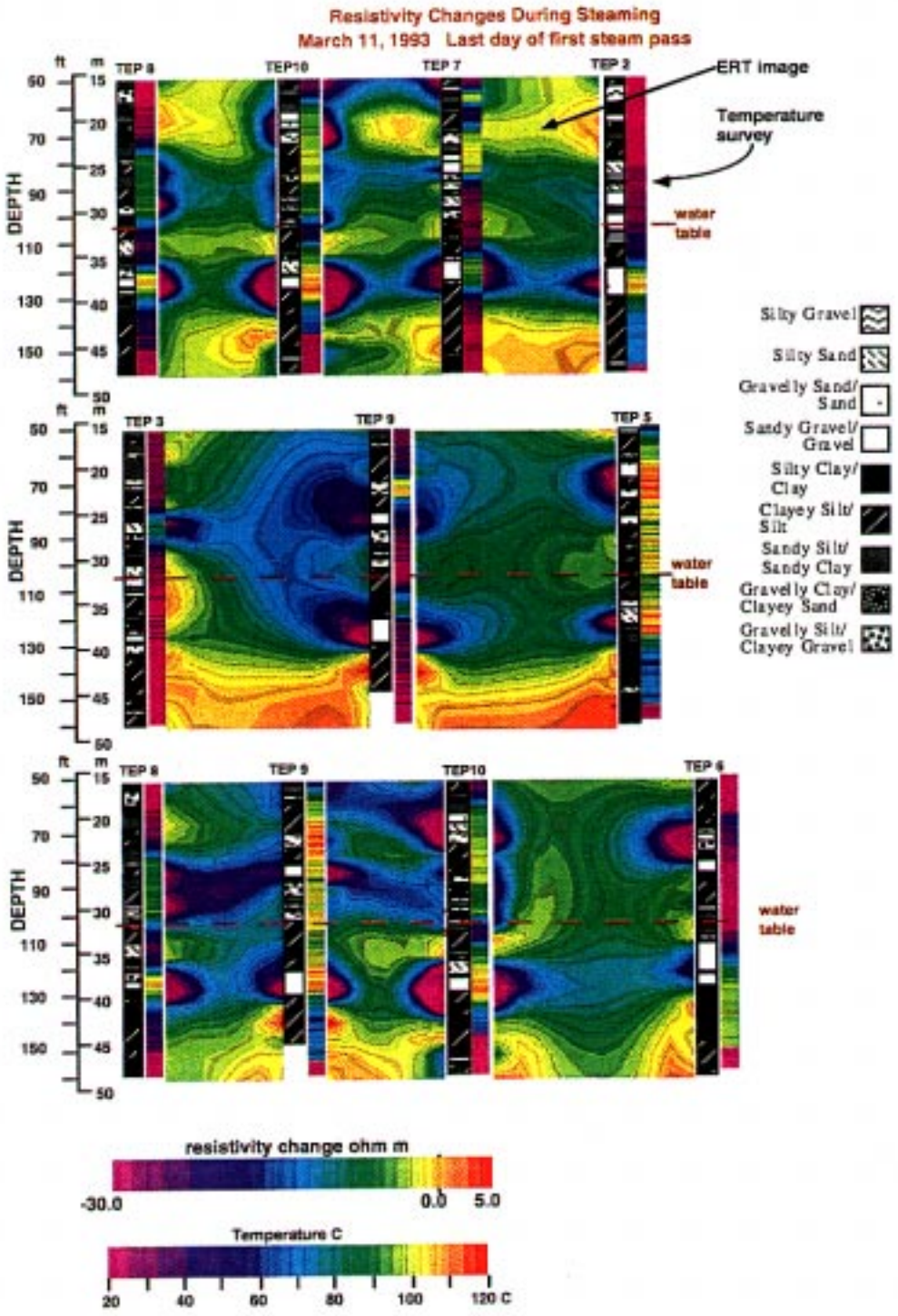

igure 13 shows the resisitivity differences measured during the last two days of ıe first steam pass. Also shown are lithologic logs and temperarture surveys ollected along the same boreholes.

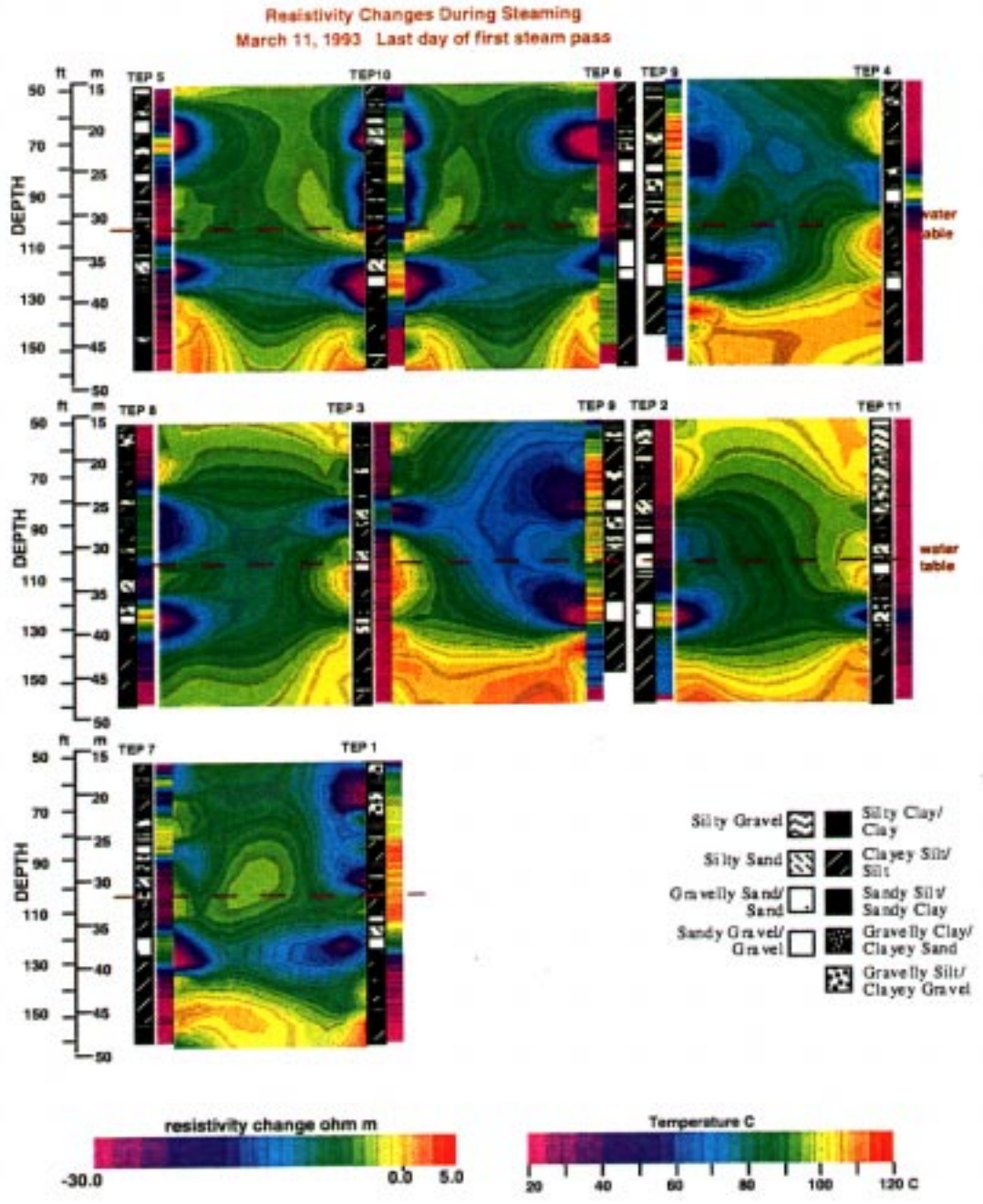

Figure 14 shows additional resisitivity differences measured during the last two days of the first steam pass. Also shown are lithologic logs and temperature surveys collected along the same boreholes.

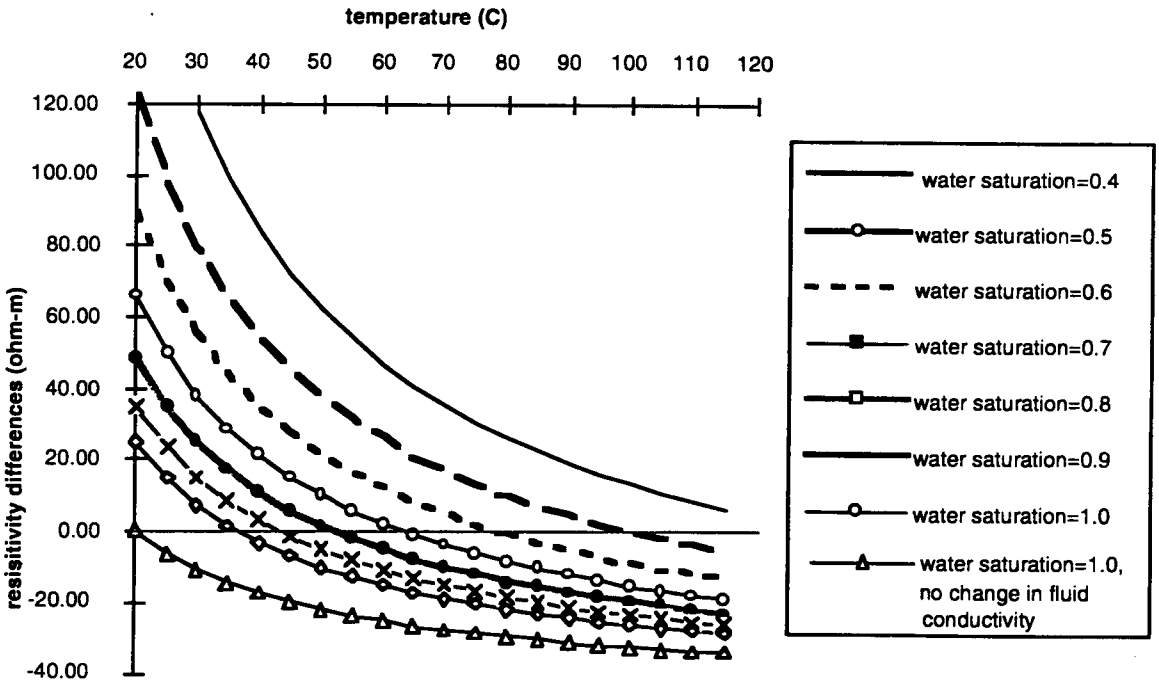

Figure 15 shows the results of calculations done using equation 1 to estimate the relationship between resistivity differences, temperature and water saturation for the case of the lower gravel steam zone during steam injection.

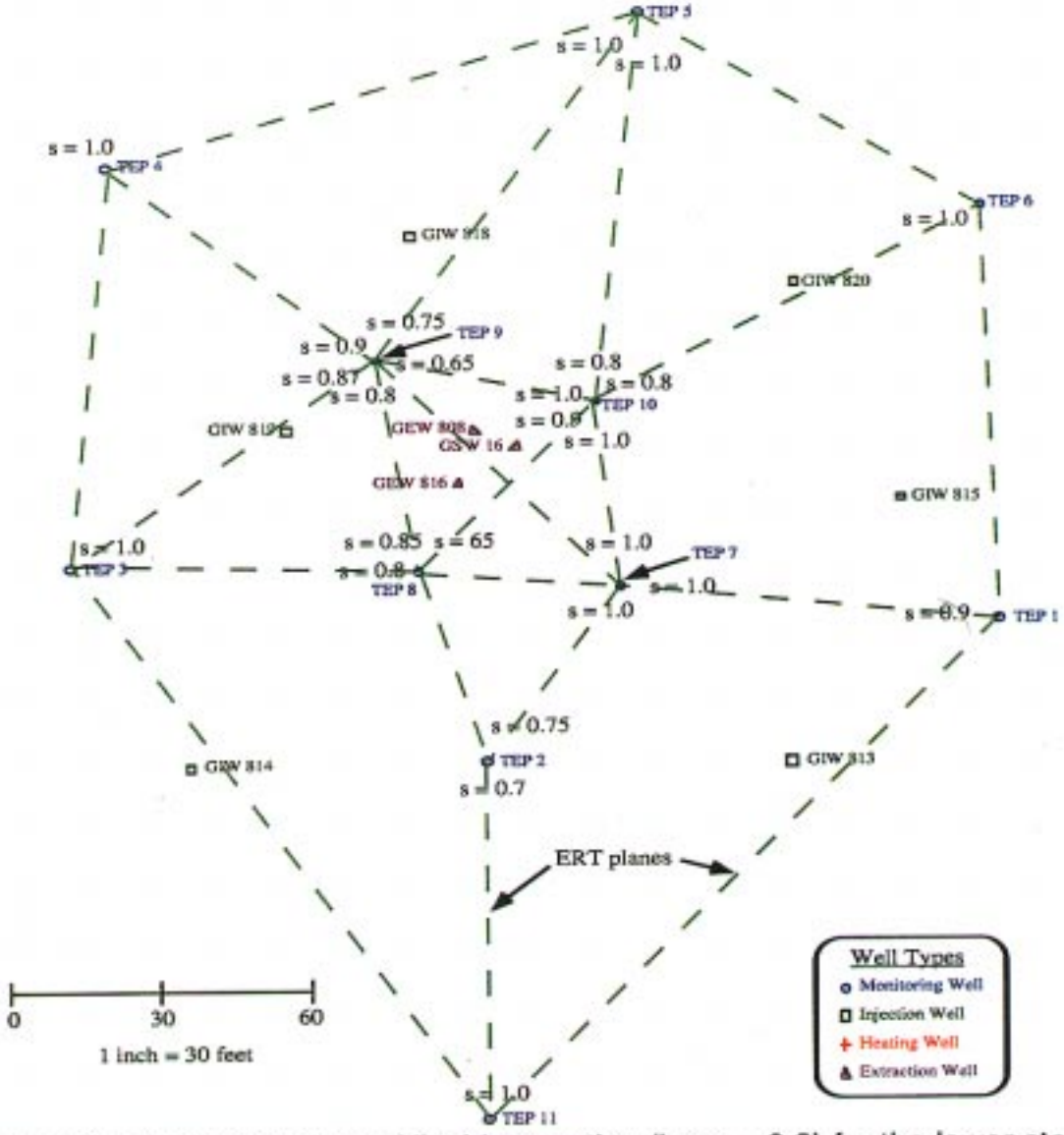

Figure 16a shows estimates of liquid saturation (i.e. s = 0.8) for the lower steam zone using the temperatures and resisitivty differences shown in Figures 13 and 14 and the resistivity differences-temperature-saturation curves shown in Figure 15. Also shown is the estimate of the location of the of the 100 C isotherm during the last day of the first steam pass.

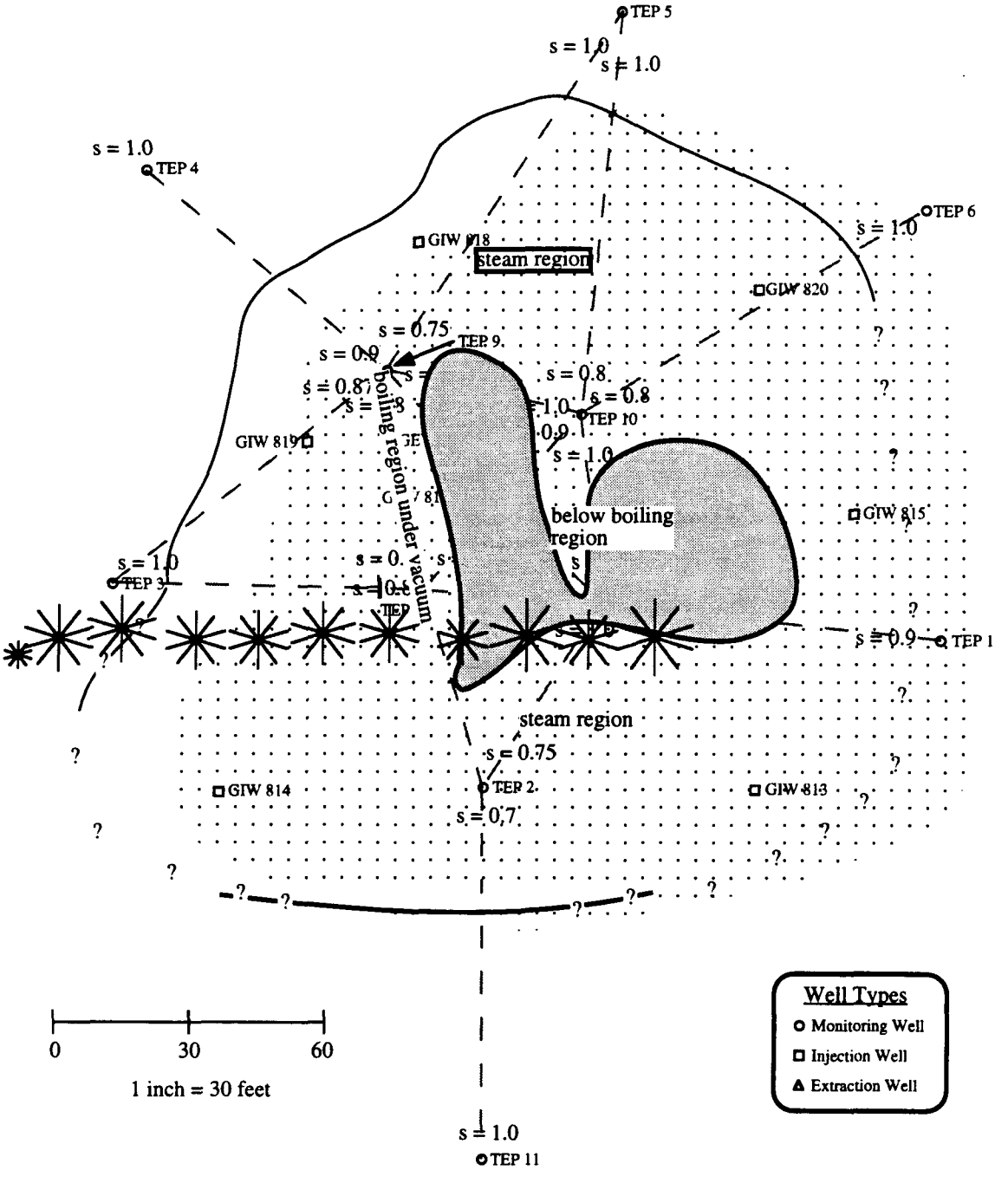
TEP 5
s = 1.0
s = 1.0
s = 1.0
TEP 4
TEP 6
s = 1.0
GIW 818
steam region
GIW 820
s = 0.75
TEP 9
s = 0.9
s = 0.8
s = 0.8
s = 0.8
s = 0.8
TEP 10
1.0
0.9
GIW 819
s = 1.0
below boiling region
GIW 815
boiling region under vacuum
s = 1.0
TEP 3
s = 0.9
TEP 1
steam region
s = 0.75
TEP 2
GIW 814
GIW 813
s = 0.7
s = 1.0
TEP 11
0
30
60
1 inch = 30 feet
Well Types
Monitoring Well
Injection Well
Extraction Well

Figure 16b

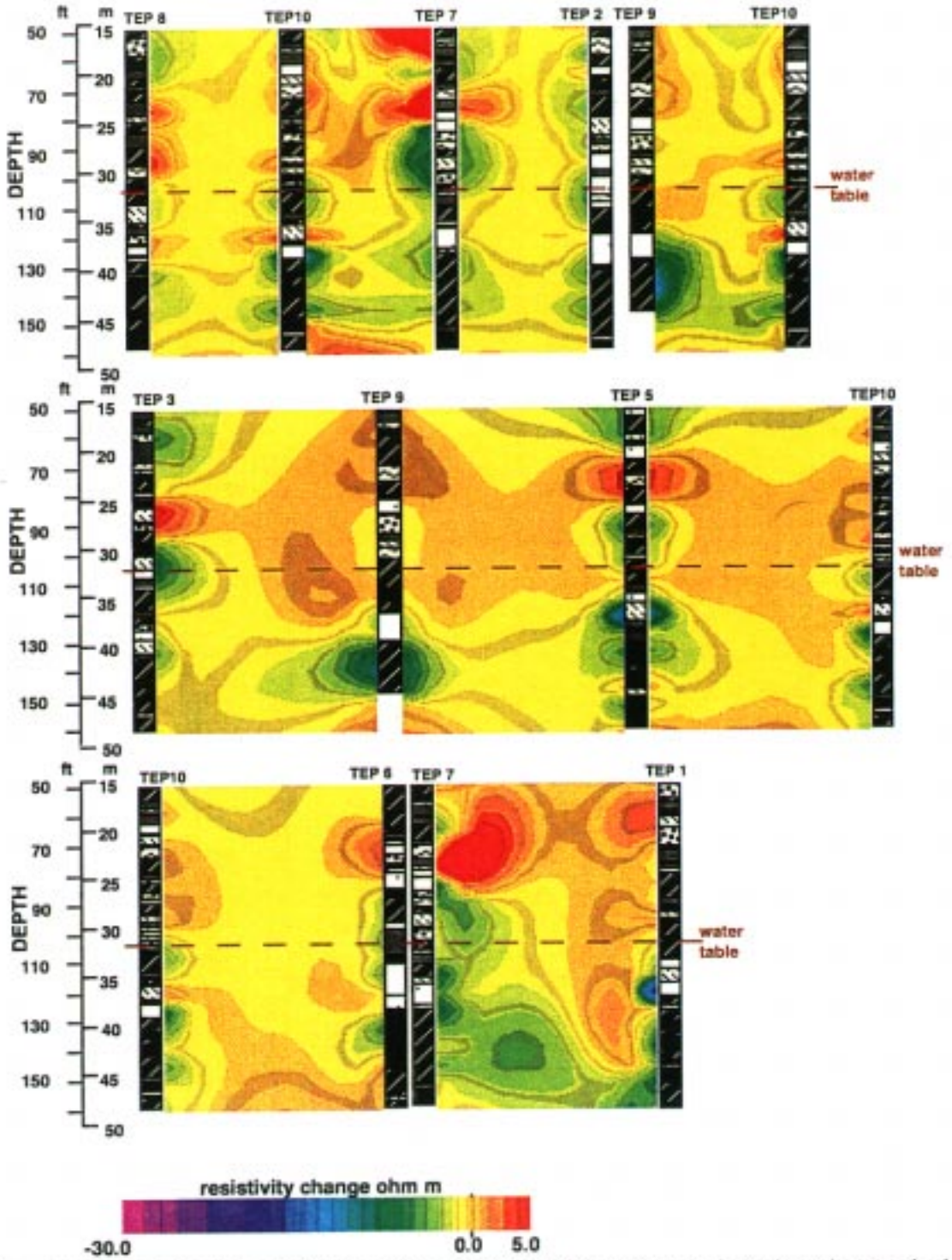

Figure 17 shows the resistivity differences which occurred during the period of no injection and extraction between the first and second steam pass. The differences shown in these figures were calculated between tomographs collected in mid May, 1993 and March 11, 1993 (the last day of steam injection -- first steam pass).

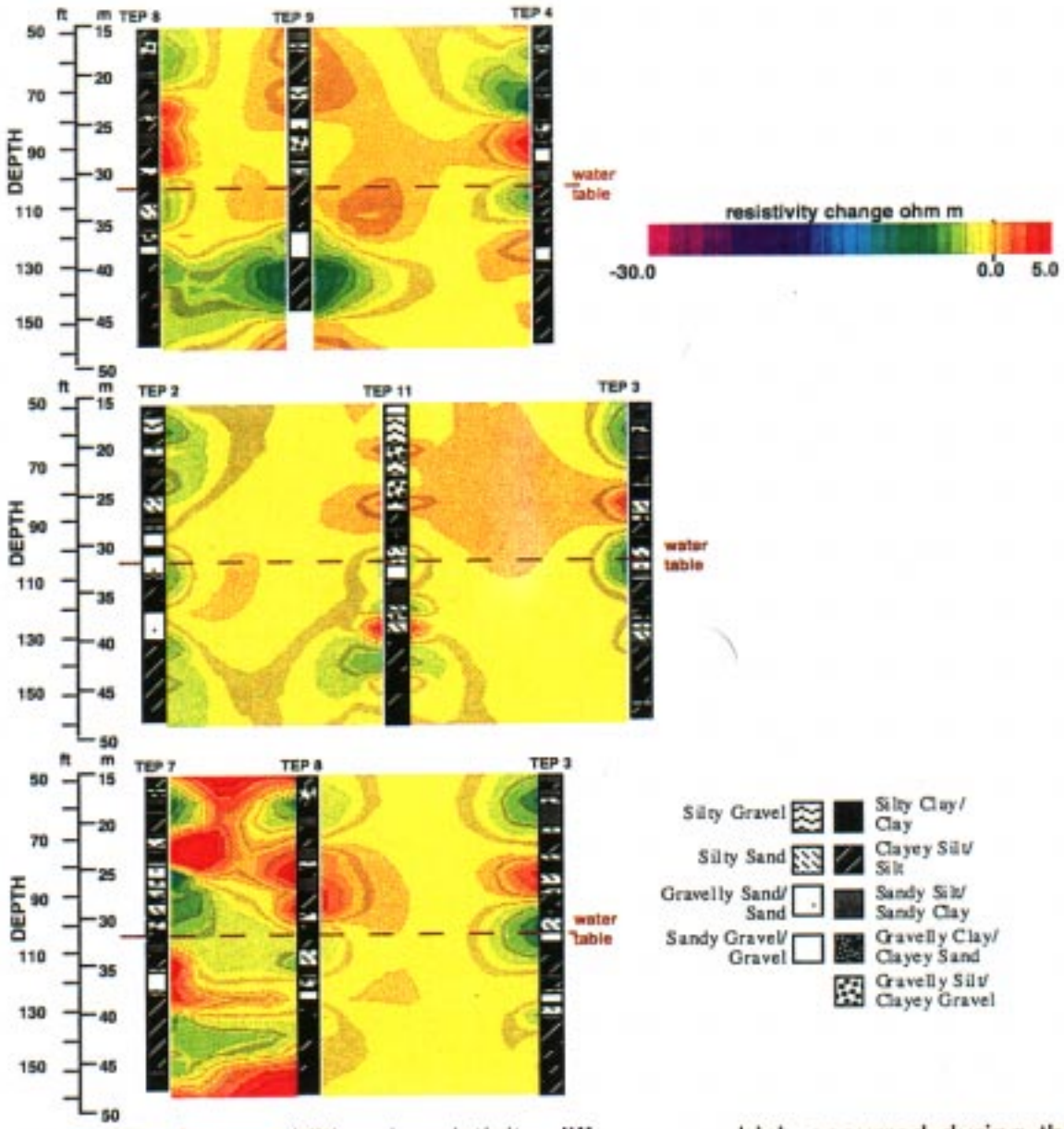

Figure 18 shows additional resistivity differences which occurred during the period of no injection and extraction between the first and second steam pass. The differences shown in these figures were calculated between tomographs collected in mid May, 1993 and March 11, 1993 (the last day of steam injection -- first steam pass).

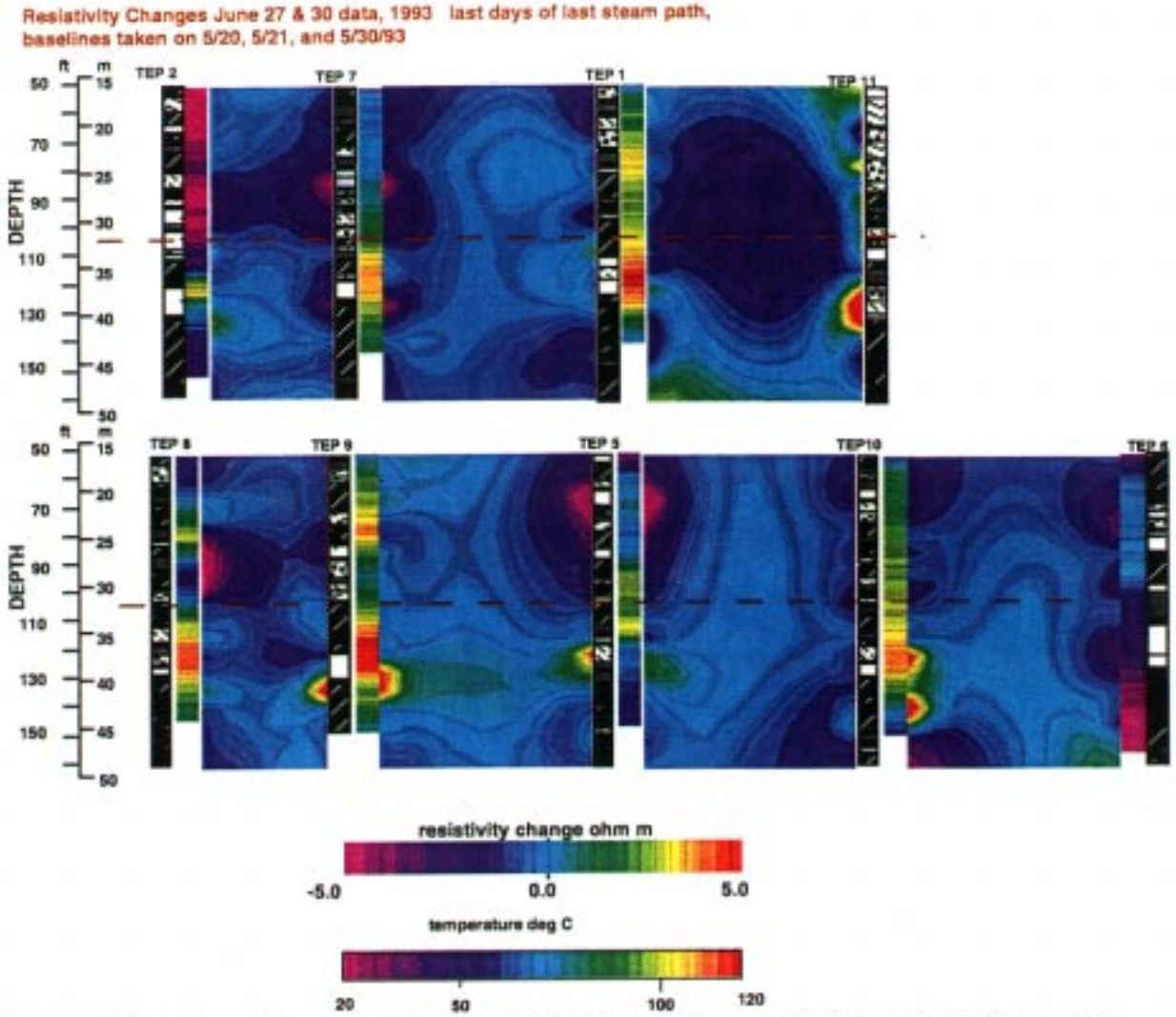

Figure 19 shows the cumulative resistivity differences which occurred during the second steam pass. The differences shown in these figures were calculated between tomographs collected June 29 and 30, 1993 (the last days of steam injection -- second steam pass) and tomographs collected prior to the start of the second steam pass.

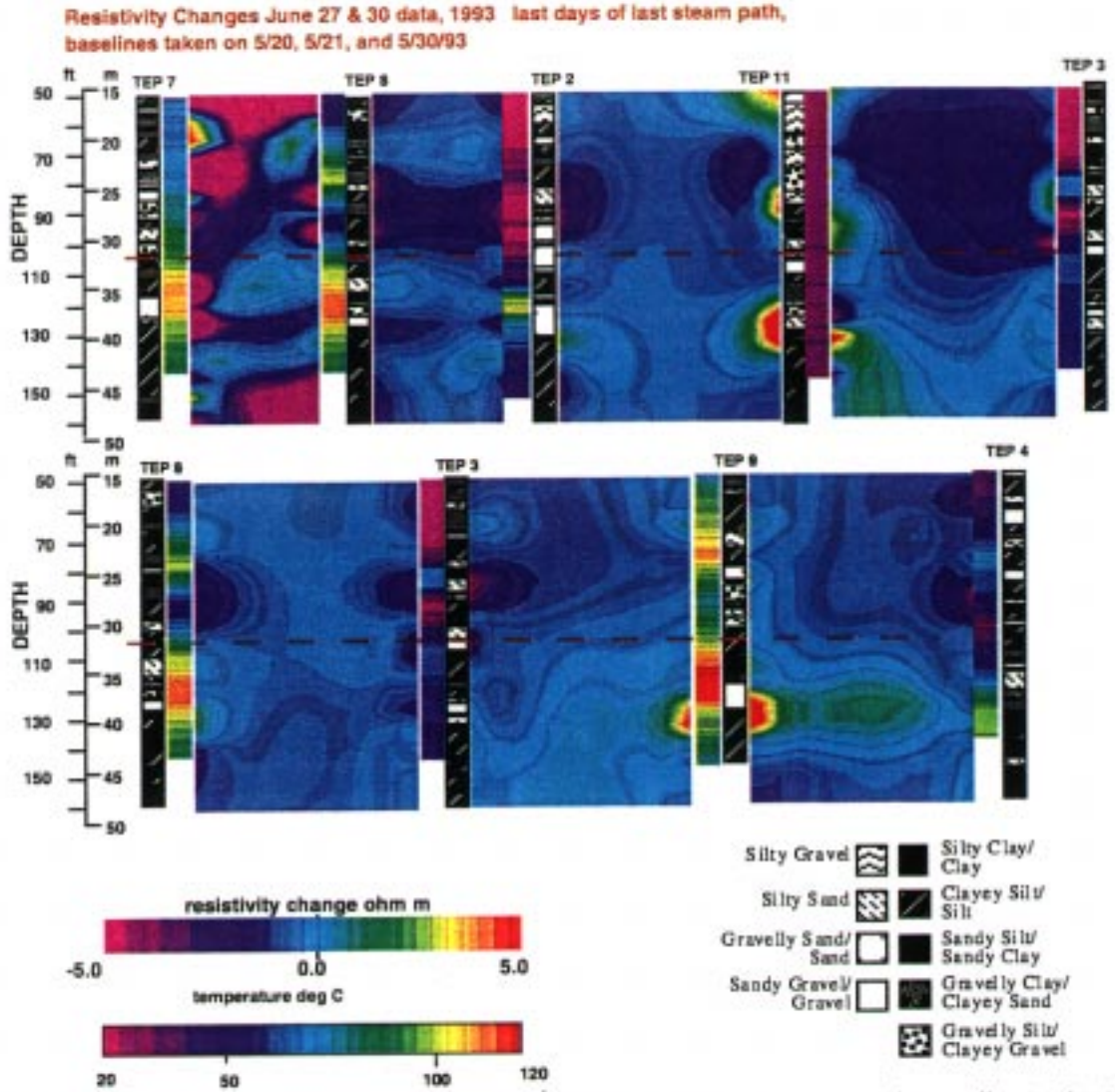

Figure 20 shows additional resistivity differences tomographs collected at the end of the second steam pass. The differences shown in these figures were calculated between tomographs collected June 29 and 30, 1993 (the last days of steam injection -- second steam pass) and tomographs collected prior to the start of the second steam pass.

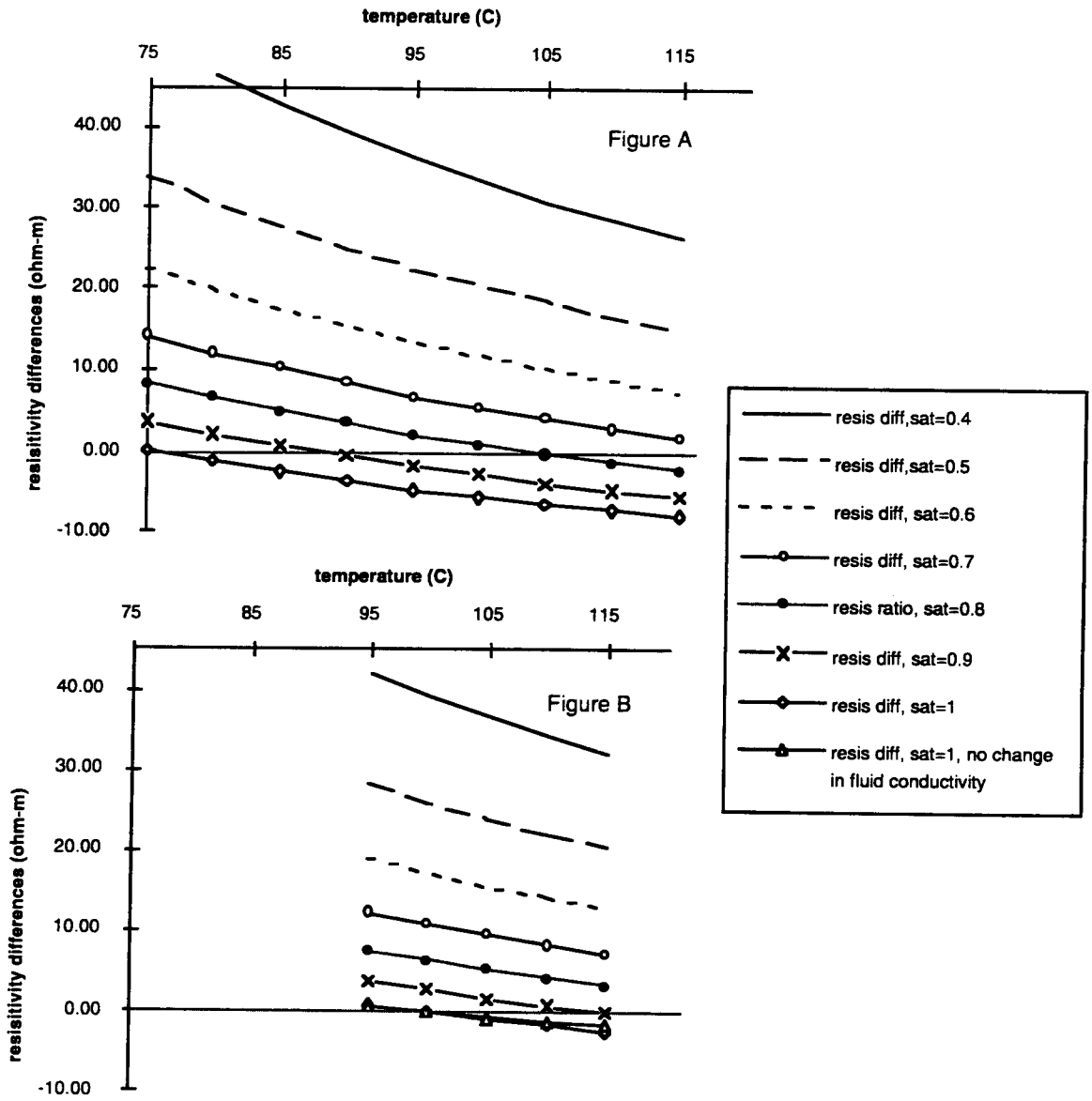

Figure 21. Figure 21 shows the results of calculations using equation 1 assuming that the initial lower steam zone temperatures was 75 C (Fig 21 A) and 95 C (Fig 21 B).

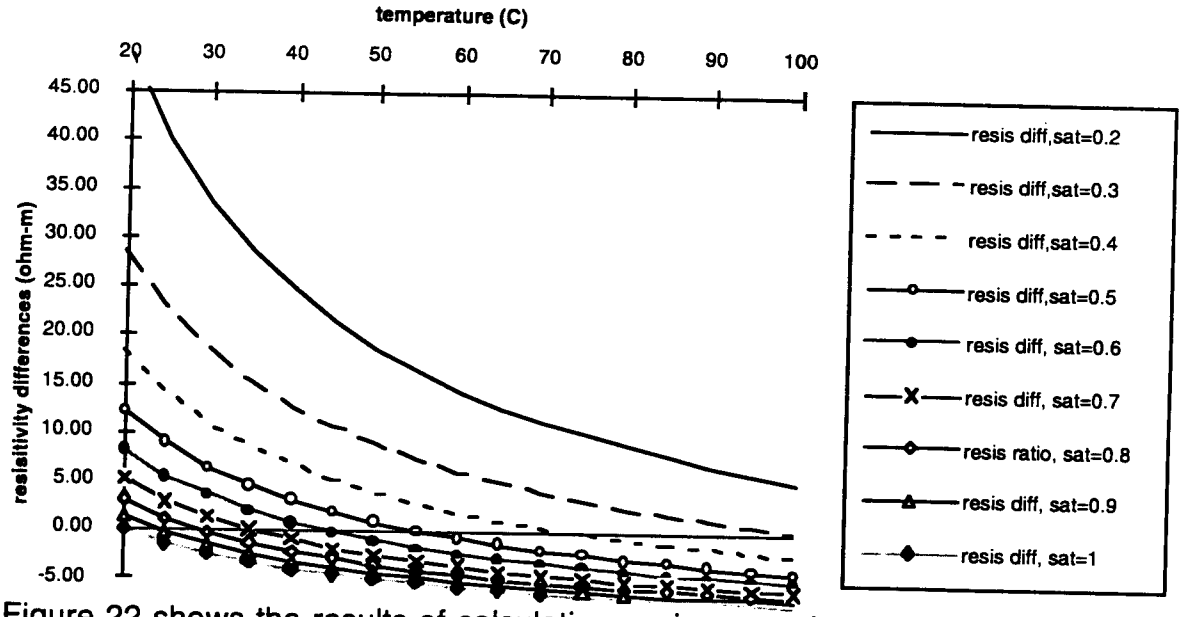

Figure 22 shows the results of calculations using equation 1 for the case of the clay layer being heated by the ohmic heating process.

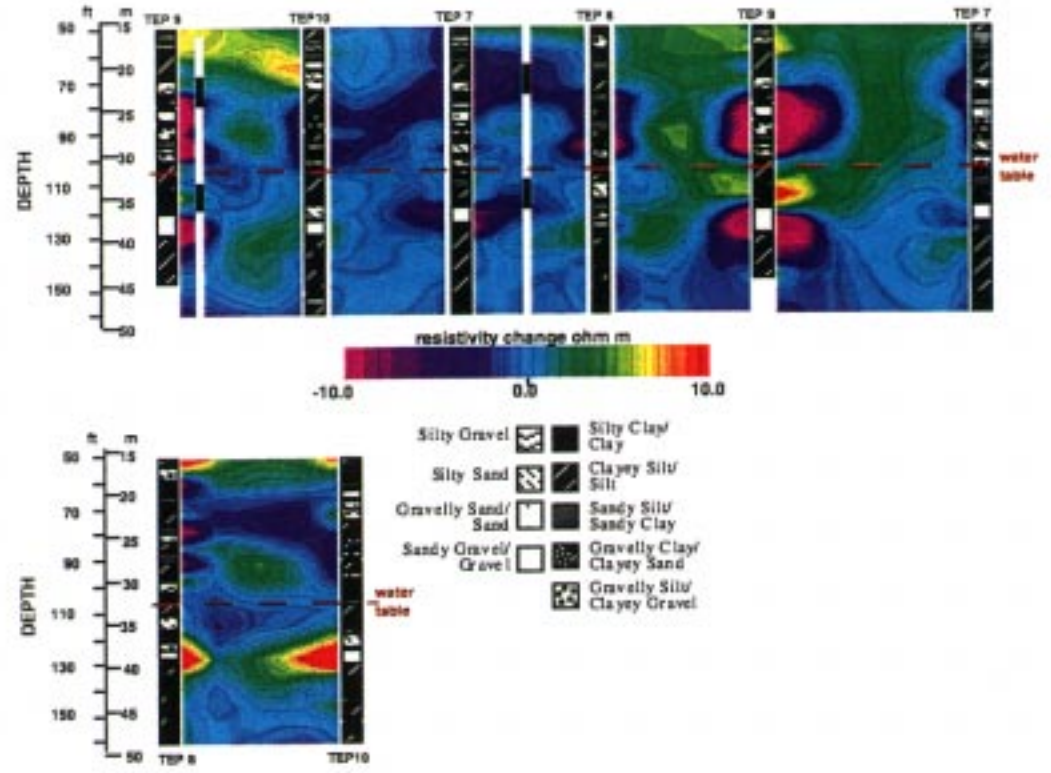

Resistivity Changes Joule Heating Dec.14-15, 1992

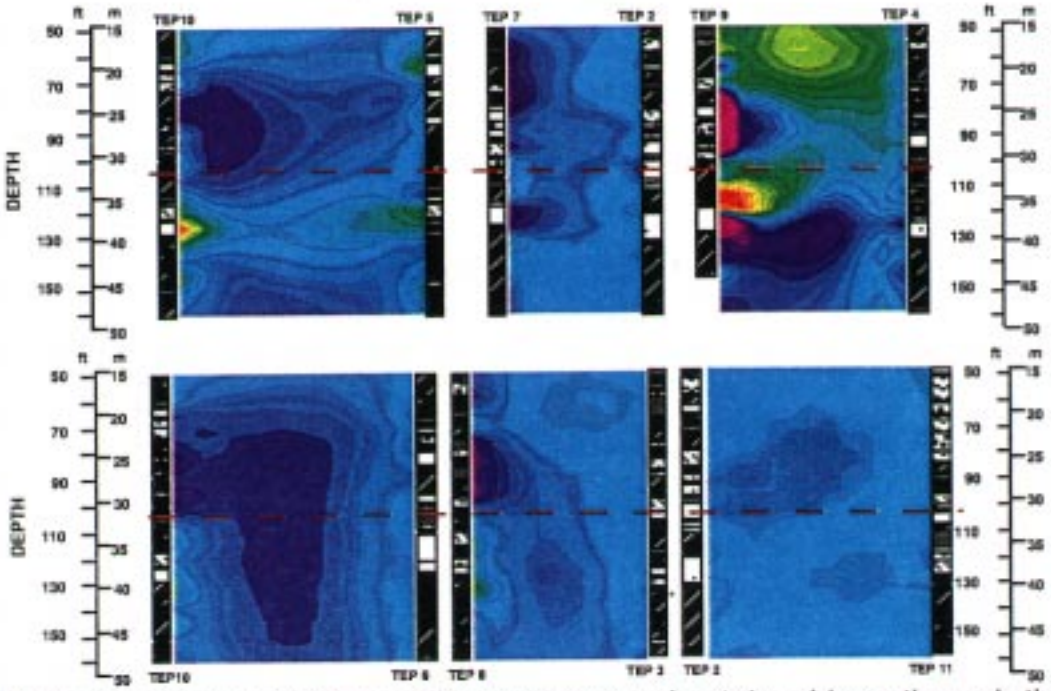

Figure 23 shows resistivity differences approximately midway through the ohmic heating phase. ERT data was collected in mid-December, 1992.

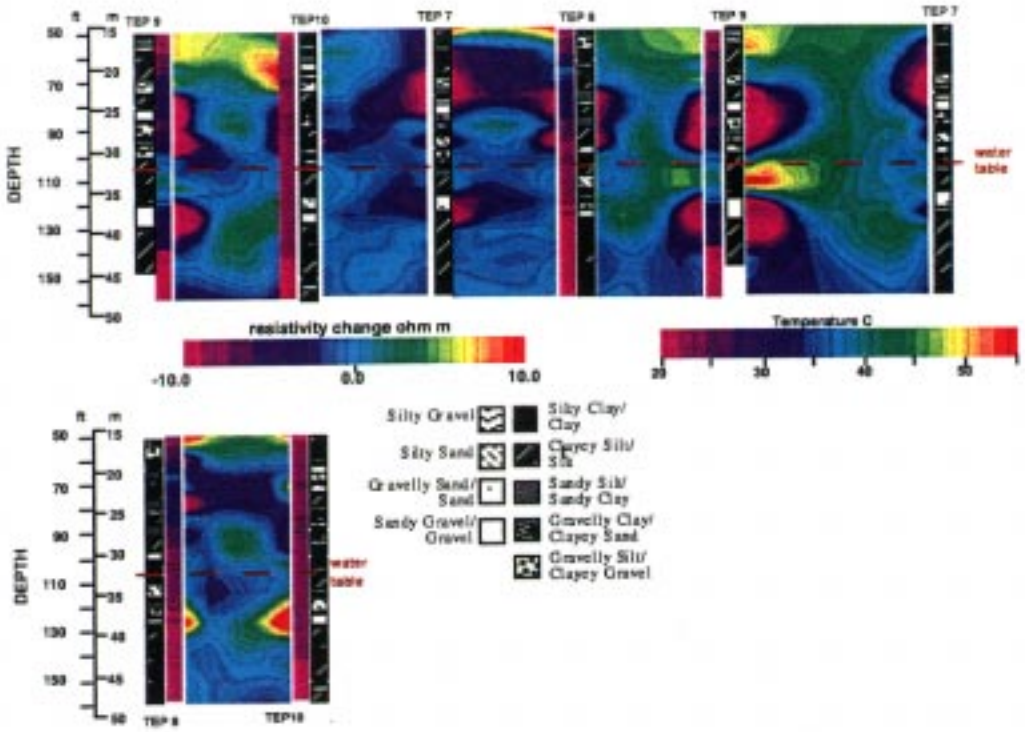

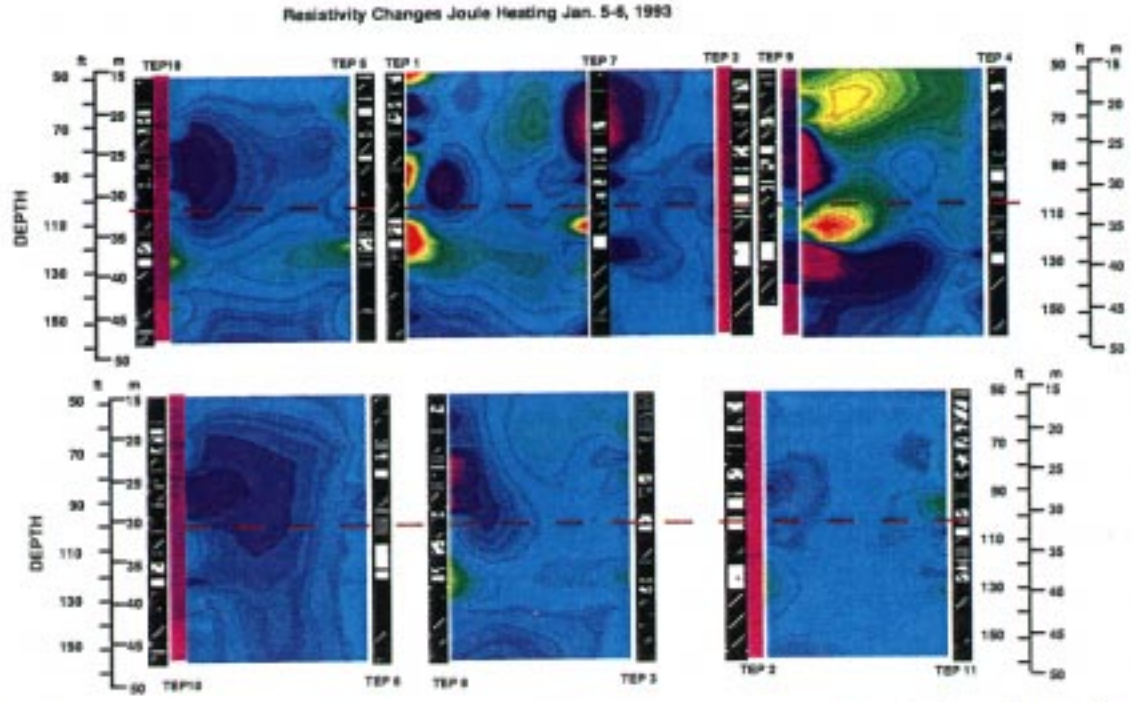

Figure 24 shows resistivity differences at the end of the ohmic heating phase. ERT data was collected in January 5-6, 1993.